A stuffed Whipple shield for the Chinese space station

Authors: Robin PUTZAR (1), ZHENG Shigui (郑世贵) (2), AN Jing (安晶) (3), Scott HOVLAND (4)

(1) Fraunhofer Institute for High-Speed Dynamics, Ernst-Mach-Institut, EMI, Ernst-Zermelo-Str. 4, 79104 Freiburg, Germany, https://orcid.org/0000-0002-1377-0763, robin.putzar@emi.fraunhofer.de

(2) China Academy of Space Technology, Beijing, 100094, People's Republic of China, wildwest77@gmail.com

(3) China Academy of Space Technology, Beijing, 100094, People's Republic of China, anjing_libra@163.com

(4) European Space Agency, European Space Research and Technology Centre (ESA/ESTEC), Keplerlaan 1, 2201 AZ Noordwijk, The Netherlands, Scott.Hovland@esa.int

Corresponding author: Robin PUTZAR, robin.putzar@emi.fraunhofer.de

Abstract

Nine successful hypervelocity impact tests between 3.1 and 7.9 km/s were performed on shield samples designated to be used onboard the future Chinese space station. Two types of shields were impact-tested: a three-layer shield consisting of a bumper, stuffing and the rear wall, and a two-layer shield. The two-layer shield configuration corresponds to the three-layer shield configuration with the bumper plate removed. The three-layer shield configuration investigated is comparable to both the ESA Columbus module debris shield and the NASA stuffed Whipple shield. A new ballistic limit equation (BLE), adopted from the NASA Nextel/Kevlar stuffed Whipple shield equation, was derived from the available experimental data for the three-layer shield. For the two-layer shield, there is not sufficient test data available for derivation of a BLE. The new BLE and a second BLE from CAST are analyzed and discussed. Overall, all BLE investigated are conservative. Considering the anticipated orbit of the Chinese space station, the CAST BLE is more conservative than the new BLE. The individual components of the shield are discussed shortly. Ballistic limit curves are given and compared against all available experimental data.

Keywords: Stuffed Whipple shield; Hypervelocity impact test; Ballistic limit equation; Basalt fabric; Aramid fabric

Highlights:

- The ballistic limit of a basalt/aramid stuffed Whipple shield was investigated experimentally.
- The shield was designed to be used onboard the future Chinese space station to be launched around 2020.
- A ballistic limit equation based on previous NASA and ESA work was adopted.
- The new ballistic limit equation allows to assess the particle impact risk of the corresponding modules.

Abbreviations

Al	aluminum
BL	ballistic limit
BLE	ballistic limit equation(s)
CAST	China Academy of Space Technology
EMI	Fraunhofer Institute for High-Speed Dynamics, Ernst-Mach-Institut
ESA/ESTEC	European Space Agency, European Space Research and Technology Centre
ISS	International Space Station
ksi	kilo pound-force per square inch; ca. 6.894 757 MPa
MDB	mesh double-bumper
MLI	multi-layer insulation
NASA	National Aeronautics and Space Administration
SW	stuffed Whipple

Nomenclature

$a_1, \ldots, a_{11}$	coefficients for Chinese BLE
c_{LV}, c_{HV}	low velocity and high velocity coefficient for BLE, respectively
d_{c}	critical diameter (perforation threshold or ballistic limit), in cm
$d_{\mathrm{c,LV}}$, $d_{\mathrm{c,IV}}$, $d_{\mathrm{c,HV}}$	critical diameter in low velocity, intermediate velocity and hypervelocity regime, respectively, in cm
d_{p}	projectile (= impactor) diameter, in cm
m_{p}	projectile (= impactor) mass
S	overall stand-off distance, in cm
s_{b}	total surface density of the mesh and the continuous bumper, in g/cm²
s_{bs}	total surface density of bumper and stuffing, in g/cm²
s_{sb}, s_{sk}	basalt and aramid layer surface density, respectively, in g/cm²
t_{b}, t_{w}	bumper plate and rear wall thickness, respectively, in cm
v	impact velocity, in km/s
v_{LV}, v_{HV}	transition velocities between low and intermediate velocity regime, and between intermediate and hypervelocity regime, respectively, in km/s
θ	impact angle, measured from the surface normal (i.e. 0° = normal or vertical impact)
ρ_{b}, ρ_{p}, ρ_{w}	densities of bumper plate, projectile (= impactor) and rear wall, respectively, in g/cm³
σ_{b}, σ_{sb}, σ_{sk}, σ_{w}	bumper plate, basalt layer, aramid layer and rear wall yield strengths, respectively, in ksi

1 Scope

Impacts of fast traveling natural micrometeoroids and anthropogenic space debris are widely considered as one of the two major threats to humankind's presence in near-Earth space. The dimensions of particles that pose an impact threat to spacecraft range from micrometer-sized micrometeoroids to the 8-ton Envisat [1]. Various types of shields were developed in the past, all of them relying on the basic principle first described by Fred Whipple [2]. The ISS, for example, is protected by many hundred shield types [3].

For the future Chinese space station to be launched around 2020, three different types of Whipple shields stuffed with aramid III and basalt fabrics were developed and tested [4]. Fraunhofer EMI was contracted by

ESA/ESTEC to perform further tests for one of the shield types tested in ref. [4], and to develop a ballistic limit equation. In this manuscript, the major results of this contractual work are summarized.

1.1 Shield description

The shield type investigated was impact tested in two configurations: a three-layer configuration that consists of a bumper, stuffing and a rear wall, and a two-layer configuration that consists of stuffing and a rear wall. The two-layer configuration corresponds to the three-layer configuration with the bumper plate removed. All targets have an additional witness plate to record residual damage during the impact tests in case the shield is perforated. This witness plate is not supposed to be present in the on-board configuration.

The bumper is 0.8 mm thick Al 3A21. The stuffing consists of one layer fireproof silica fiber cloth (beta cloth), three layers basalt fabric, three layers aramid III fabric, and MLI. The basalt layers are 0.096 g/cm² fabric made from 9 µm diameter BWF-9 fibers, manufactured by Zhejiang Shi Jin Basalt Fiber Co., Ltd. (浙江石金玄武岩纤维有限公司). The aramid III layers are 0.06 g/cm² fabric made from 15 µm diameter FB1100 fibers, manufactured by Sichuan Hui Teng Technology Co., Ltd. (四川辉腾科技有限公司). The rear wall is 2.5 mm thick Al 5A06. The witness plate is 1.0 mm thick Al 5A06. The nominal distances inside the shield are: bumper to stuffing 60 mm, bumper to rear wall 80 mm, rear wall to witness plate 50 mm. Figure 1 shows sample photographs of the three-layer configuration targets. Table 4 lists the shield materials and their properties.

The bumper plate is also used as a radiator plate.

Basalt and aramid III fabrics were chosen as stuffing materials based on the results of previously conducted hypervelocity impact experiments, taking into account both engineering criteria and availability in China. During those previous experiments, the protective performance of the following materials was compared: basalt, carbon fiber, silicon carbide, Kevlar, aramid III and other materials.

Previous investigations concluded that placing the stuffing close to the rear wall improved protective performance [5]. In ref. [5], the best protective performance was achieved for the stuffing being placed at two third of the overall spacing behind the bumper plate. With the current configuration, the fabric is supposed to cover the module wall directly, without the need of a supporting structure of the fabric.

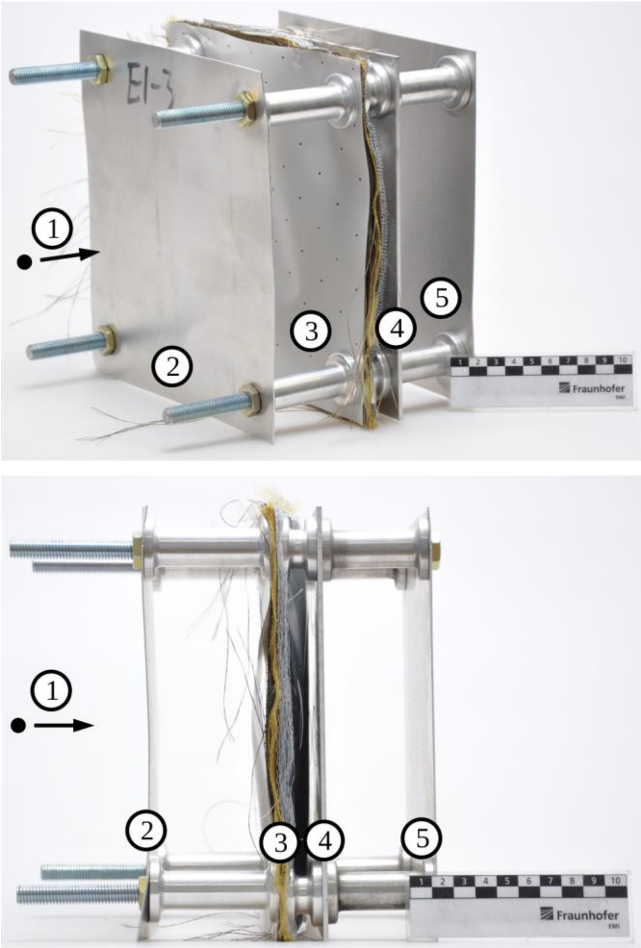

Figure 1: Photograph of target EI-3, oblique view (top) and EI-2, side view (bottom), showing the three-layer configuration. The scale in the images is in centimeters. 1 – impact direction, 2 – bumper plate (only present in three-layer configuration), 3 – stuffing, 4 – rear wall, 5 – witness plate (not present in on-board configuration).

2 Comparing with shield types from literature

Usually, the development of a ballistic limit equation is preceded by many impact tests. The ballistic limit equation for the ESA Columbus module debris shield, for example, was developed using more than 100 experimental data points [6]. The NASA stuffed Whipple shield equation is also backed by extensive impact testing [7]. Since the amount of tests available in the experimental campaign presented was limited, analyses that have been performed by other research groups for comparable shield types were utilized to support the development of the ballistic limit equation. Three existing shield types were considered as comparable: the ESA Columbus module debris shield, the NASA Nextel/Kevlar stuffed Whipple (SW) shield, and the NASA mesh double-bumper (MDB) shield. Figure 2 shows those three shield configurations compared to the tested shield (in three-layer configuration).

The debris shield for ESA’s Columbus module of the ISS was developed by Alenia Aerospazio (now Thales Alenia Space) and Fraunhofer EMI [6, 8-11]. The shield is comprised of an aluminum bumper, a second bumper with Nextel, Kevlar-epoxy and multi-layer insulation (MLI), and an aluminum rear wall. Two shield configurations were developed: for the cylindrical section and for the cone section. In Figure 2, the cylindrical section shield is shown. The NASA Nextel/Kevlar stuffed Whipple shield was developed for the ISS [12-14]. Several configurations of this shield exist. All of them comprise an aluminum bumper, a second bumper with Nextel, Kevlar and sometimes an aluminum mesh, and an aluminum rear wall. The mesh double-bumper (MDB) shield was also developed by NASA [15, 16]. This shield comprises an aluminum mesh as first bumper, a second continuous aluminum bumper, a high-strength fabric intermediate layer (third bumper) and an aluminum rear wall. Modified versions of this shield are actually used to protect areas of the ISS [13].

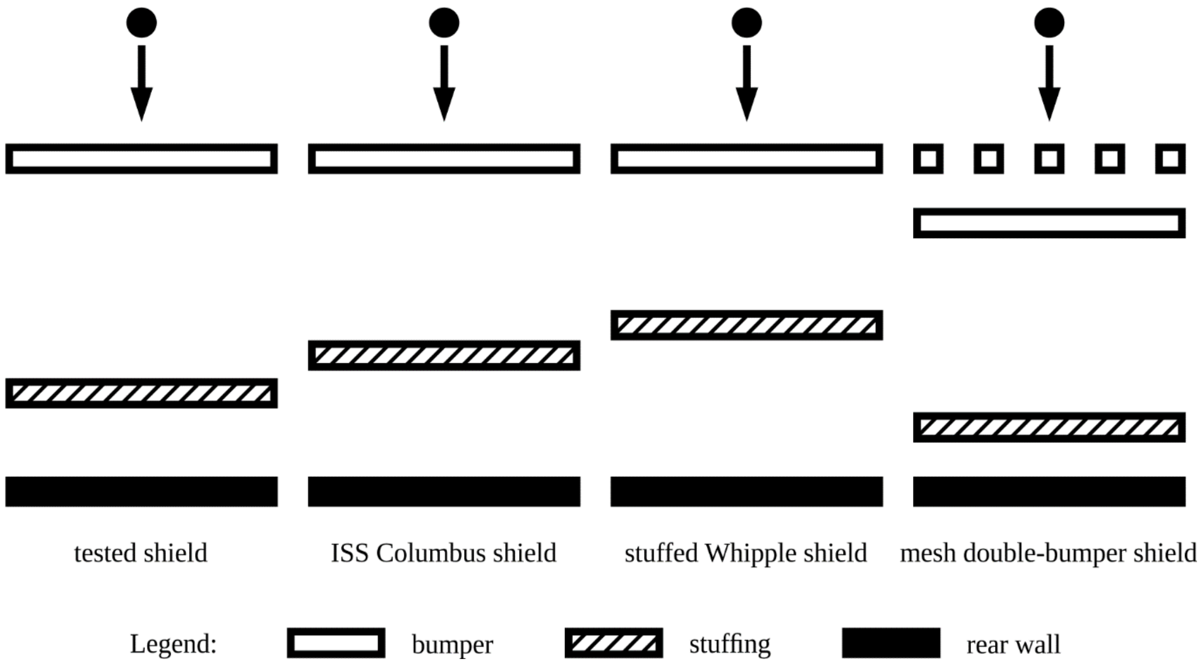

Figure 2: Configurations of tested shield (in three-layer configuration) and comparable shields from literature. The relative placement of the components within the shields is to scale, but the absolute size of the shields is normalized.

2.1 Ballistic limit equations

Ballistic limit equations (BLE) for spacecraft shields allow calculation of the perforation threshold or critical diameter d_c as function of the impactor properties and shield parameters. They are usually given for three regimes of the impact velocity v [17]: the low velocity regime with no or little fragmentation of the impacting particle, the hypervelocity regime with full fragmentation and partial melt and vaporization of the impacting particle, and, between the two, an intermediate or shatter velocity regime. Here, the transition velocities are denoted v_LV (low to intermediate) and v_HV (intermediate to hypervelocity). The critical diameters in the three velocity regimes are denoted $d_\mathrm{c,LV}$ (low velocity regime), $d_\mathrm{c,IV}$ (intermediate velocity regime) and $d_\mathrm{c,HV}$ (hypervelocity regime). In the intermediate velocity regime, all BLE considered use a linear interpolation:

$$d_\mathrm{c,IV} = d_\mathrm{c,LV}(v = v_\mathrm{LV}) \cdot \frac{v_\mathrm{HV} - v}{v_\mathrm{HV} - v_\mathrm{LV}} + d_\mathrm{c,HV}(v = v_\mathrm{HV}) \cdot \frac{v - v_\mathrm{LV}}{v_\mathrm{HV} - v_\mathrm{LV}} \quad . \tag{1}$$

In summary, the overall ballistic limit equation is given by

$$d_\mathrm{c} = \begin{cases} d_\mathrm{c,LV} & v \leq v_\mathrm{LV} \\ d_\mathrm{c,IV} & v_\mathrm{LV} < v < v_\mathrm{HV} \\ d_\mathrm{c,HV} & v_\mathrm{HV} \leq v \end{cases} \quad . \tag{2}$$

2.1.1 Chinese basalt/aramid stuffed Whipple shield

The transition velocities of the BLE defined in ref. [4] for the investigated shield are defined by $v_\mathrm{LV} = 2.6\ \frac{\mathrm{km}}{\mathrm{s}} \cdot (\cos\theta)^{-\frac{1}{2}}$ and $v_\mathrm{HV} = 6.5\ \frac{\mathrm{km}}{\mathrm{s}} \cdot (\cos\theta)^{-\frac{3}{4}}$. The critical diameter d_c is given by

$$d_{\mathrm{c,LV}} = a_1 \left(t_\mathrm{w} + t_\mathrm{b} \left(\frac{\sigma_\mathrm{b}}{\sigma_\mathrm{w}}\right)^{a_2} + \frac{s_\mathrm{sb}}{\rho_\mathrm{w}} \left(\frac{\sigma_\mathrm{sb}}{\sigma_\mathrm{w}}\right)^{a_2} + \frac{s_\mathrm{sk}}{\rho_\mathrm{w}} \left(\frac{\sigma_\mathrm{sk}}{\sigma_\mathrm{w}}\right)^{a_2} \right) \left(\frac{\rho_\mathrm{w}}{\rho_\mathrm{p}}\right)^{a_3} \left(\frac{\rho_\mathrm{p} \cdot (v \cdot \cos\theta)^2}{\sigma_\mathrm{w}}\right)^{a_4} , \tag{3}$$

$$d_{\mathrm{c,HV}} = a_5 \left(t_\mathrm{b}^{a_6}\, t_\mathrm{w}^{a_7}\, S^{1-a_6-a_7} + a_8 \left(\frac{s_\mathrm{sb}}{\rho_\mathrm{w}}\right)^{a_9} \left(\frac{s_\mathrm{sk}}{\rho_\mathrm{w}}\right)^{1-a_9} \right) \left(\frac{\rho_\mathrm{w}}{\rho_\mathrm{p}}\right)^{a_{10}} \left(\frac{\rho_\mathrm{p} \cdot (v \cdot \cos\theta)^2}{\sigma_\mathrm{w}}\right)^{a_{11}} , \tag{4}$$

with bumper plate and rear wall thicknesses t_b and t_w in cm, bumper plate, rear wall and projectile densities ρ_b, ρ_w and ρ_p in g/cm³, basalt and aramid layer surface densities s_sb, s_sk in g/cm², bumper plate, basalt layer, aramid layer and rear wall yield strengths σ_b, σ_sb, σ_sk, σ_w in ksi and overall stand-off distance S in cm. Nominal values are $t_\mathrm{b} = 0.08$ cm, $t_\mathrm{w} = 0.25$ cm, $\rho_\mathrm{b} = \rho_\mathrm{w} = 2.67\ \mathrm{g/cm^3}$, $s_\mathrm{sb} = 0.096\ \mathrm{g/cm^2}$, $s_\mathrm{sk} = 0.06\ \mathrm{g/cm^2}$, $\sigma_\mathrm{b} = 14$ ksi, $\sigma_\mathrm{sb} = 273$ ksi, $\sigma_\mathrm{sk} = 421$ ksi, $\sigma_\mathrm{w} = 47$ ksi and $S = 8$ cm. The coefficients a_1 to a_{11} are [4]: $a_1 = 0.67977$, $a_2 = 0.22523$, $a_3 = 0.24552$, $a_4 = -0.223$, $a_5 = 1.02$, $a_6 = 0.20646$, $a_7 = 0.387$, $a_8 = 1.346$, $a_9 = 0.53972$, $a_{10} = 0.27$, $a_{11} = -0.25$.

The shape of the Chinese ballistic limit equation was derived in ref. [18]. This approach is outlined in Appendix A. The parameters a_1 to a_{11} were derived using a differential evolution algorithm [19, 20] and experimental data. This algorithm is outlined in Appendix B.

2.1.2 ESA Columbus module debris shield

The ballistic limit equation for the ESA Columbus module debris shield is modified from [12] with mainly new coefficients derived from the experiments [6]. The transition velocities of this BLE are defined by $v_\mathrm{LV} = 2.7\ \frac{\mathrm{km}}{\mathrm{s}} \cdot (\cos\theta)^{-\frac{1}{2}}$ and $v_\mathrm{HV} = 6.5\ \frac{\mathrm{km}}{\mathrm{s}} \cdot (\cos\theta)^{-\frac{1}{3}}$. The critical diameter d_c is given by

$$d_{\mathrm{c,LV}}(v) = c_\mathrm{LV} \cdot v^{-\frac{2}{3}} \quad , \tag{5}$$

$$d_{\mathrm{c,HV}}(v) = c_\mathrm{HV} \cdot v^{-\frac{1}{3}} \tag{6}$$

with the coefficients c_LV and c_HV being derived from the experiments.

2.1.3 NASA Nextel/Kevlar stuffed Whipple shield

The BLE for the NASA SW shield is given in [13, 14, 17, 7] (although in [7] there seems to be a misprint in the factor coefficient for the hypervelocity regime). The original definition in [12] deviates somewhat from those later formulations. The transition velocities of this BLE are defined by $v_\mathrm{LV} = 2.6\ \frac{\mathrm{km}}{\mathrm{s}} \cdot (\cos\theta)^{-\frac{1}{2}}$ and $v_\mathrm{HV} = 6.5\ \frac{\mathrm{km}}{\mathrm{s}} \cdot (\cos\theta)^{-\frac{3}{4}}$. The critical diameter d_c is given by

$$d_{\mathrm{c,LV}}(v) = 2.35 \cdot \left(t_\mathrm{w} \cdot \left(\frac{\sigma_\mathrm{w}}{40\ \mathrm{ksi}}\right)^{\frac{1}{2}} + 0.37 \frac{\mathrm{cm}^3}{\mathrm{g}} \cdot s_\mathrm{bs} \right) \cdot \rho_\mathrm{p}^{-\frac{1}{2}} \cdot v^{-\frac{2}{3}} \cdot (\cos\theta)^{-\frac{4}{3}} \quad , \tag{7}$$

$$d_{\mathrm{c,HV}}(v) = 0.6 \cdot (t_\mathrm{w} \rho_\mathrm{w})^{\frac{1}{3}} \cdot \rho_\mathrm{p}^{-\frac{1}{3}} \cdot v^{-\frac{1}{3}} \cdot (\cos\theta)^{-\frac{1}{2}} \cdot S^{\frac{2}{3}} \cdot \left(\frac{\sigma_\mathrm{w}}{40\ \mathrm{ksi}}\right)^{\frac{1}{6}} \tag{8}$$

with rear wall thickness t_w in cm, rear wall and projectile densities ρ_w and ρ_p in g/cm³, total surface density of bumper and stuffing (including MLI) s_bs in g/cm², rear wall yield strength σ_w and overall shield spacing S in cm.

2.1.4 NASA mesh double-bumper shield

The BLE for the NASA MDB shield is given in [13, 16, 17, 7]. The transition velocities of this BLE are defined by $v_{\mathrm{LV}} = 2.8\ \frac{\mathrm{km}}{\mathrm{s}} \cdot (\cos\theta)^{-\frac{1}{2}}$ and $v_{\mathrm{HV}} = 6.4\ \frac{\mathrm{km}}{\mathrm{s}} \cdot (\cos\theta)^{-\frac{1}{3}}$. The critical diameter d_{c} is given by

$$d_{\mathrm{c,LV}}(v) = 2.2 \cdot \left(t_{\mathrm{w}} \cdot \left(\frac{\sigma_{\mathrm{w}}}{40\ \mathrm{ksi}}\right)^{\frac{1}{2}} + 0.37 \frac{\mathrm{cm}^3}{\mathrm{g}} \cdot (s_{\mathrm{b}} + s_{\mathrm{sk}}) \right) \cdot \rho_{\mathrm{p}}^{-\frac{1}{2}} \cdot v^{-\frac{2}{3}} \cdot (\cos\theta)^{-\frac{5}{3}} \quad , \tag{9}$$

$$d_{\mathrm{c,HV}}(v) = 0.6 \cdot (t_{\mathrm{w}}\rho_{\mathrm{w}})^{\frac{1}{3}} \cdot \rho_{\mathrm{p}}^{-\frac{1}{3}} \cdot v^{-\frac{1}{3}} \cdot (\cos\theta)^{-\frac{1}{3}} \cdot S^{\frac{1}{2}} \cdot \left(\frac{\sigma_{\mathrm{w}}}{40\ \mathrm{ksi}}\right)^{\frac{1}{6}} \tag{10}$$

with rear wall thickness t_{w} in cm, rear wall and projectile densities ρ_{w} and ρ_{p} in g/cm³, total surface density of both the mesh and the continuous bumper s_{b} and of the high-strength fabric intermediate layer s_{sk} in g/cm², rear wall yield strength σ_{w} and overall shield spacing S in cm.

2.1.5 Differences of ballistic limit equations

The ESA Columbus BLE and the two NASA BLE are very similar. For the ESA BLE this is no surprise, since this equation was derived from the NASA SW shield BLE. The NASA SW shield BLE and the NASA MDB shield BLE were derived by the same team consecutively, which may explain the similarity. The main differences between those three BLE are slightly different transition velocities, different exponent coefficients of the angular dependencies, different exponent coefficients of the spacing, and the slightly different factor coefficients in the two velocity regimes.

The Chinese ballistic limit equation deviates substantially from all other BLE. In the hypervelocity regime, $d_{\mathrm{c,HV}} \sim v^{-\frac{1}{2}}$ for the Chinese BLE, while $d_{\mathrm{c,HV}} \sim v^{-\frac{1}{3}}$ for all other BLE. According to the current understanding, the Chinese BLE therefore will yield conservative results for very high velocities.

Comparing the other three BLE, the differences in transition velocities and exponent coefficients can be explained by different phenomenological behavior of the individual shield types during the impact process. The main reason for the different transition velocities are the different shock pressures generated in the impacting particle. The mesh double-bumper shield is especially successful in this respect; therefore, the transition velocity to hypervelocity is the lowest.

The exponent coefficients for the angle dependency $\cos\theta$ and for the spacing S were derived through fitting to experimental data. The same applies to the factor coefficients. Those coefficients account for the different performance of the shields.

2.2 Comparison

All of the shield types described above comprise a first aluminum bumper (or a double bumper in case of the MDB shield), a second stuffing layer and an aluminum rear wall. In the following, the differences between the three shields to the Chinese shield tested are described, and the implications for the impact process and the corresponding BLE are analyzed.

2.2.1 Basalt fibers

One of the major differences between the Chinese shield and other shields is that the stuffing uses basalt fabric instead of Nextel fabric. Nextel is a ceramic fiber, while basalt is a rock material. Nextel 312 (which is the Nextel type used in the ESA Columbus module shield and the NASA Nextel/Kevlar stuffed Whipple shield) consists of 62.5 wt% Al_2O_3, 24.5 wt% SiO_2 and 13 wt% B_2O_3 [21]. Basalt fibers typically consist of 42 – 56 wt% SiO_2, 11 – 18 wt% Al_2O_3, 7 – 12 wt% CaO, 4 – 11 wt% MgO plus other compounds [22]. Basalt fibers are said to have mechanical properties similar to those of glass fibers [22]. Basalt fibers were previously investigated in Whipple or stuffed Whipple shield configurations [23-25]. Table 1 compares the mechanical properties of Nextel 312, basalt fibers and glass fibers.

The influence of basalt fabrics on the projectile fragments is unknown. Nextel 312 fabrics generate high shock pressures in impacting particles, higher than an equivalent weight aluminum bumper [17]. No work that compares basalt to either Nextel or glass fabrics (with respect to hypervelocity impacts) could be found in the literature.

Table 1: Properties of Nextel 312, basalt fibers and glass fibers, from [17, 21, 22, 26, 27].

Property	Nextel 312	Basalt fibers	E-glass
Density	2.7 – 2.8 g/cm³	2.6 – 2.8 g/cm³	2.56 g/cm³
Tensile strength	1.6 – 1.7 GPa	2.8 – 4.8 GPa	1.4 – 2.5 GPa
Elastic modulus	150 – 152 GPa	85 – 110 GPa	76 GPa

2.2.2 Comparison to other debris shield types

The Columbus shield is the most similar to the Chinese shield of all three shields considered here. Apart from the use of basalt fabrics instead of Nextel, an important difference is the mass division between the Nextel/basalt layers and the aramid layers. This will influence the behavior of the projectile fragments at the stuffing. A less important difference concerns the exact types of materials involved, i. e. the aluminum alloy types and the type of aramid used. The location of the stuffing in the Chinese shield corresponds to the location of the stuffing in the cone configuration.

As the major differences between the Chinese shield and the Columbus shield is the stuffing material (basalt instead of Nextel), the general impact processes should be similar for both shields. Differences in impact behavior between basalt and Nextel may influence the transition velocity between the intermediate and the hypervelocity regime. This can be evaluated by the experiments, especially by analyzing the rear wall failure behavior. A rear wall failure around 6.5 km/s which is mainly caused by the impulsive load of the fragment cloud and not by impacting fragments would indicate that the transition velocity is around or below 6.5 km/s.

The major difference between the Chinese shield and the NASA SW shield is again the stuffing material: basalt fabric instead of Nextel fabric. Additionally, the stuffing placement within the shield is different ($\approx 0.25 \cdot S$ in front of the rear wall instead of in the middle between bumper plate and rear wall), and the mass division between the Nextel/basalt layers and the aramid layers is different. Despite these differences, the general impact process of the NASA SW shield should be similar to the impact process of the Chinese shield, as is the case with the Columbus shield. The reasoning given in the previous section holds true also for the NASA SW shield.

The major differences between the Chinese shield and the NASA MDB shield are the double bumper and the composition of the stuffing. According to refs. [15] and [16], the fragmentation on a wire mesh is more dispersive than an impact into the same surface density bumper. The double-bumper causes an additional shock in the projectile fragments, further increasing the molten or vaporized fraction of the projectile. This explains the slightly reduced hypervelocity transition velocity when compared to the NASA SW shield. In general, the NASA MDB shield is less similar to the Chinese shield than both the ESA Columbus shield and the NASA stuffed Whipple shield.

3 Hypervelocity impact testing

Impact testing was performed at Fraunhofer EMI’s light-gas gun facilities, where the on-orbit particle environment can be simulated in ground tests. The facilities at Fraunhofer EMI provide the best possible hypervelocity impact performance in terms of impact velocity range and projectile size range in Europe, and represent the state of the art in current test capabilities. At the Fraunhofer Ernst-Mach-Institut, four high-velocity impact facilities are used for the simulation of space debris and micrometeoroid impacts on spacecraft components and planetary bodies. The impact facilities are closed indoor two-stage light-gas guns [28-30].

Nine successful tests were performed on the eight targets. One target was impacted twice, with the impact location of the subsequent experiment chosen so that the pre-damage did not affect the new damage. Table 2 lists the experimental results. Projectiles were spheres made of 99.9 % aluminum. The residual pressure in the target chamber was 12 kPa (120 mbar). The experiments were conducted at room temperature (between 22 and 23 °C).

After each impact test, the damage to the shield caused by the impacting projectile was recorded, described and analyzed. The major result of each test is the damage to the rear wall, which is described in more detail in the next section. The failure criterion for the shield was defined as either perforation or detached spallation from the rear wall. Detached spallation was not observed in any of the tests, therefore failure ("> BL") corresponds to perforation of the rear wall. Table 2 also lists the measurements performed at the individual targets prior and after impact testing. If no accuracy is given, the last digit has an accuracy of ±1. Hole sizes and areas were measured in horizontal and vertical direction with both values given in the table. Damage values for experiment 5817 are given in brackets, because the damage was caused by the impact of the projectile as well as by subsequent impact of a piece of the sabot as explained in the following section.

3.1 Rear wall damage descriptions

The rear wall of experiment 5807 is not perforated. It features some impact craters, and deposit on the front side. The rear wall rear side features one larger and one smaller bulge. The maximum bulge height is 0.3 mm.

The rear wall of experiment 5808 is perforated. It features one hole, some impact craters, and deposit on the front side. The rear wall rear side is bent rearward with a maximum height of ca. 2.3 mm.

The rear wall of experiment 5810 is perforated. It features one hole with four cracks. The rear wall features deposit but no visible impact craters, suggesting complete melt of the projectile. The rear wall rear side is bent rearward with a maximum height of ca. 20 – 25 mm (depending on the reference point).

The rear wall of experiment 5811 is not perforated. It features deposit but no visible impact craters, suggesting complete melt of the projectile. The rear wall rear side is bent rearward with a maximum height of ca. 11 – 14 mm (depending on the reference point).

The rear wall of experiment 5816 is perforated. It features one large hole with two longer cracks in horizontal and two very short cracks in vertical direction, some impact craters, and deposit. The hole is in the center of the rear wall. The rear wall rear side is bent rearward with a maximum height of ca. 12 – 13 mm (depending on the reference point).

The damage to the target of experiment 5817 was caused by the impact of the projectile as well as by subsequent impact of a piece of the sabot. Analyses of the high-speed video show that the projectile fragments caused perforation of the rear wall before fragments of the sabot could reach the rear wall. However, the rear wall damage was caused by both the projectile impact and the sabot impact. Therefore, the damage measurement values in Table 2 are given in brackets. The rear wall of experiment 5817 is perforated. It features one larger hole with three short cracks and one small hole, some impact craters, and deposit. The larger hole is in the center of the rear wall. The small hole is close to the lower edge of the rear wall. The rear wall rear side features some bulges and is bent rearward with a maximum height of ca. 9 – 10 mm (depending on the reference point).

Table 2: Experimental results and target measurements prior and after impact testing. The row “result” indicates if the test was below (“< BL”) or above (“> BL”) the ballistic limit; hole sizes and areas are given as horizontal × vertical.

Experiment	5807	5808	5810	5811	5816	5817	5814	5815	5819
Target name	EI-1	EI-2	EI-3	EI-4	EI-7	EI-8	EI-5	EI-6	EI-6
Nominal projectile diameter (in mm)	4.1	5.0	6.6	6.0	6.4	6.0	2.0	2.8	2.5
Projectile mass (in mg)	98.7	177.6	409.5	302.2	358.3	299.9	11.8	30.3	20.9
Impact angle	0°	0°	0°	0°	45°	45°	0°	0°	0°
Impact velocity (in km/s, ±0.03)	3.93	3.70	6.35	6.00	6.25	6.38	7.94	7.12	7.58
Result	< BL	> BL	> BL	< BL	> BL	> BL	< BL	> BL	> BL
Target layers	3	3	3	3	3	3	2	2	2
Bumper plate thickness (in mm, ±0.02)	0.75	0.74	0.74	0.74	0.74	0.74	–	–	–
Rear wall thickness (in mm, ±0.02)	2.43	2.43	2.43	2.44	2.44	2.43	2.43	2.44	2.44
Witness plate thickness (in mm, ±0.02)	0.92	0.92	0.92	0.91	0.91	0.91	0.93	0.91	0.91
Distance bumper plate – beta cloth (in mm)	56	61	59	59	56	57	–	–	–
Distance beta cloth – rear wall (in mm)	–	–	–	–	–	–	24	23	23
Distance bumper plate – rear wall (in mm)	79.7	80.3	79.3	79.2	80.2	80.0	–	–	–
Distance rear wall – witness plate (in mm)	49.6	50.1	48.5	48.1	49.7	48.3	48.8	50.3	49.9
Holes in rear wall	0	1	1	0	1	(2)	0	2	1
Largest hole size in rear wall (in mm × mm)	–	5.3 × 5.3	17 × 14	–	9 × 9	(4.3 × 3.3)	–	3.0 × 4.5	1.3 × 1.3
Area with impact craters in rear wall (in mm × mm)	14 × 8	30 × 42	–	–	22 × 20	(21 × 25)	8 × 7	7 × 8	8 × 5
Area with cracks in rear wall (in mm × mm)	–	–	37 × 52	–	21 × 13	(10 × 9)	–	–	–

The rear wall of experiment 5814 is not perforated. It features deposit and very few impact craters, with one central crater being the largest. The rear wall rear side features a single bulge with a maximum height of ca. 0.2 mm. The target for experiment 5814 was pre-damaged by failed experiment 5812. In experiment 5812, the projectile did not reach the target. Instead, the target was hit by a small fragment of the piston at low speed (ca. 500 – 1000 m/s). The stuffing was partially perforated. The rear wall was undamaged after experiment 5812. The impact location for experiment 5814 was chosen so that the pre-damage did not affect the new damage.

The rear wall of experiment 5815 is perforated. It features one large and one very small hole, some impact craters, and deposit. The rear wall rear side is bent rearward with a maximum height of ca. 3 – 4 mm.

The rear wall of experiment 5819 is perforated. It features one very small hole, some impact craters, and deposit. The rear wall rear side features the hole and three small bulges. The crater rim of the hole has a maximum height of ca. 1.1 mm. The target for experiment 5819 was pre-damaged by experiments 5812 and

5814. The impact location for experiment 5819 was chosen so that the pre-damage did not affect the new damage.

Post-test pictures of the targets are published in [31].

4 Analyses and discussion

4.1 Shield components

The purpose of the bumper plate is to break up incoming particles. This break-up is achieved by shock pressures induced during the impact process, which depend heavily on the material density and thermodynamic properties (heat capacity, melting point etc.) of the bumper material [17]. The bumper material used is aluminum alloy 3A21. The usual bumper material for spacecraft shields is aluminum alloy 6061 T6. The thermodynamic properties of 3A21 were not raised during the activity, but the difference to 6061 T6 will be not significant. The most significant difference between the two alloys is the tensile strength. 3A21 has a comparatively low tensile strength. According to Christiansen [17], the tensile properties of the bumper material are not very significant. Therefore, the performance of a 3A21 bumper should be comparable to a 6061 T6 bumper.

The purpose of the stuffing material is to further shock and slow down the fragments of the fragment cloud that is generated by the impact on the bumper plate. The difference of the stuffing composition and placement is discussed in Section 2.2 above, raising the question on the transition velocity between the intermediate and hypervelocity regime v_{HV}. The rear walls from the two impact tests 5810 and 5811 at 6.2 ± 0.2 km/s show no impact craters, suggesting complete melt of the projectile and bumper fragments. Given the small amount of impact tests actually performed, it was chosen to stick with the value of the transition velocity as used by the NASA SW shield (6.5 km/s). Since complete melt in the experiments at Fraunhofer EMI was already achieved at 6.0 km/s (experiment 5811), the transition velocity to hypervelocity might be lower than that. Before modifying the BLE accordingly, this finding should be substantiated using dedicated impact experiments.

The purpose of the rear wall is to stop the remaining fragments. At high velocities (starting from ca. 6.5 km/s for normal impacts), the kinetic energy transferred to internal energy upon impact is sufficient to partially melt and evaporate the impacting particle. Therefore, the predominant loading on the rear wall is impulsive loading from finely dispersed and partially molten or evaporated fragments. The most important characteristic of the rear wall therefore is its ability to withstand impulsive loading. The rear wall should be ductile with a high tensile strength [17]. The rear wall material used is aluminum alloy 5A06. The yield strength of this material provided by CAST is 47 ksi (≈ 324 MPa). Values in the literature vary between 110 MPa and 340 MPa [32-36]. The rear wall material used for the ISS Columbus shield is aluminum alloy 2219-T851 [6]. The yield strength of this material is 51 ksi (≈ 352 MPa) [7].

4.2 Ballistic limit equation for the three-layer shield

4.2.1 Derivation

The experimental data available for the investigated shield comprises six impact tests performed in the frame of this contract plus 13 impact tests performed by CAST [4]. Therefore, the data basis for derivation of a BLE is comparatively limited.

The NASA SW BLE (which also is the basis for the Columbus shield) was therefore selected as basis for a new BLE, with the coefficients adjusted to match the experimental data. This effectively implies that the physical effects during impacts on the two shield types are comparable.

The transition velocities are defined by $v_{\mathrm{LV}} = 2.6\ \frac{\mathrm{km}}{\mathrm{s}} \cdot (\cos\theta)^{-\frac{1}{2}}$ and $v_{\mathrm{HV}} = 6.5\ \frac{\mathrm{km}}{\mathrm{s}} \cdot (\cos\theta)^{-\frac{3}{4}}$. The critical diameter d_{c} is given by

$$d_{\mathrm{c,LV}}(v) = c_{\mathrm{LV}} \cdot \left(t_{\mathrm{w}} \cdot \left(\frac{\sigma_{\mathrm{w}}}{40\ \mathrm{ksi}}\right)^{\frac{1}{2}} + 0.37 \frac{\mathrm{cm}^3}{\mathrm{g}} \cdot s_{\mathrm{bs}} \right) \cdot \rho_p^{-\frac{1}{2}} \cdot v^{-\frac{2}{3}} \cdot (\cos\theta)^{-\frac{4}{3}} \quad , \tag{11}$$

$$d_{\mathrm{c,HV}}(v) = c_{\mathrm{HV}} \cdot (t_{\mathrm{w}}\, \rho_{\mathrm{w}})^{\frac{1}{3}} \cdot \rho_{\mathrm{p}}^{-\frac{1}{3}} \cdot v^{-\frac{1}{3}} \cdot (\cos\theta)^{-\frac{1}{2}} \cdot S^{\frac{2}{3}} \cdot \left(\frac{\sigma_{\mathrm{w}}}{40\ \mathrm{ksi}}\right)^{\frac{1}{6}} \quad . \tag{12}$$

Here, d_{c} is the critical or ballistic limit diameter in cm, v is the projectile impact velocity in km/s, θ is the impact angle, t_{w} is the rear wall thickness in cm, ρ_{w} is the rear wall density in g/cm³, σ_{w} is the rear wall yield strength, s_{bs} is the total surface density of the bumper and the stuffing in g/cm², ρ_{p} is the projectile density in g/cm³, and S is the overall shield spacing in cm. c_{LV} and c_{HV} are fitting parameters for adjustment to the experimental data.

Table 3: Experimental data used to fit the BLE parameters c_{LV} and c_{HV}. The column “result” indicates if the test was below (“< B.L.”) or above (“> B.L.”) the ballistic limit.

Source	Nominal projectile diameter	Projectile mass	Effective projectile diameter	Impact angle	Impact velocity	Result
	[mm]	[mg]	[mm]		[km/s]	
EMI 5807	4.1	98.7 ± 0.1	4.118 ± 0.006	0°	3.93 ± 0.02	< BL
EMI 5808	5.0	117.6 ± 0.1	5.008 ± 0.007	0°	3.70 ± 0.02	> BL
EMI 5810	6.6	409.5 ± 0.1	6.617 ± 0.009	0°	6.35 ± 0.02	> BL
EMI 5811	6.0	302.2 ± 0.1	5.979 ± 0.008	0°	6.00 ± 0.02	< BL
EMI 5816	6.4	358.3 ± 0.1	6.328 ± 0.008	45°	6.25 ± 0.02	> BL
EMI 5817	6.0	299.9 ± 0.1	5.964 ± 0.008	45°	6.38 ± 0.02	> BL
CAST SW2-1	4.25	111.3	4.239	0°	3.03	> BL
CAST SW2-2	3.75	75.3	3.722	0°	3.156	< BL
CAST SW2-3	4.0	92.5	3.986	0°	3.165	< BL
CAST SW2-4	3.0	39.2	2.994	30°	3.132	< BL
CAST SW2-5	3.25	49.9	3.245	30°	3.124	< BL
CAST SW2-6	3.5	62.1	3.490	30°	2.89	> BL
CAST SW2-7	6.0	318.3	6.017	0°	6.715	< BL
CAST SW2-8	6.5	401.3	6.501	0°	6.512	< BL
CAST SW2-9	7.0	500.5	6.997	0°	6.364	> BL
CAST SW2-10	6.75	449.6	6.752	0°	6.571	> BL
CAST SW2-11	6.0	317.4	6.012	30°	6.64	< BL
CAST SW2-12	6.5	401.6	6.502	30°	6.645	< BL
CAST SW2-13	6.75	449.8	6.753	30°	6.503	> BL

Table 3 lists the experimental data used to derive the two fitting parameters c_{LV} and c_{HV}. Besides the nominal projectile diameter, the effective projectile diameter is given, which is calculated from the projectile mass m_{p} using $\sqrt[3]{\frac{6 \cdot m_{\mathrm{p}}}{\pi \cdot \rho_{\mathrm{p}}}}$ and assuming a projectile density of (2.70 ± 0.01) g/cm³ for the experiments at EMI, and 2.79 g/cm³ for the experiments at CAST.

Table 4 lists the material properties of the shields required for calculation of the ballistic limit equations. For the experiments at Fraunhofer EMI, the measured data was used for thicknesses and spacing. For the experiments at CAST, the nominal data given in Ref. [4] is used.

Table 4: Shield material properties for the three-layer target.

Component	Property		Value	Source	Comment
Projectile	Density	ρ_{p}	2.70 g/cm³	Nominal	For EMI tests
	Density	ρ_{p}	2.79 g/cm³	CAST	For CAST tests
Bumper plate	Material		Al 3A21	CAST	
	Thickness	t_{b}	0.074 cm	EMI	For EMI tests
	Thickness	t_{b}	0.08 cm	Nominal	For CAST tests
	Density	ρ_{b}	2.67 g/cm³	CAST	
	Surface density	s_{b}	0.1976 g/cm²	Calculated	For EMI tests
	Surface density	s_{b}	0.2136 g/cm²	Calculated	For CAST tests
	Yield strength	σ_{b}	14 ksi	CAST	
Beta cloth	Surface density		0.0163 ± 0.0003 g/cm²	EMI	
Basalt fabric	Surface density	s_{sb}	0.096 g/cm²	CAST	
	Yield strength	σ_{sb}	273 ksi	CAST	
Aramid fabric	Surface density	s_{ck}	0.06 g/cm²	CAST	
	Yield strength	σ_{ck}	421 ksi	CAST	
MLI	Surface density		0.041 ± 0.001 g/cm²	EMI	
Bumper and stuffing	Surface density	s_{bs}	0.370 g/cm²	Calculated	For EMI tests
	Surface density	s_{bs}	0.386 g/cm²	Calculated	For CAST tests
Rear wall	Material		Al 5A06	CAST	
	Thickness	t_w	0.243 cm	EMI	For EMI tests
	Thickness	t_w	0.25 cm	Nominal	For CAST tests
	Density	ρ_w	2.67 g/cm³	CAST	
	Surface density	s_{w}	0.6488 g/cm²	Calculated	For EMI tests
	Surface density	s_{w}	0.6675 g/cm²	Calculated	For CAST tests
	Yield strength	σ_{w}	47 ksi	CAST	
Whole target	Spacing	S	8.0 cm	Nominal	For EMI tests
	Spacing	S	7.75 cm	Nominal	For CAST tests
	Surface density		1.02 g/cm²	Calculated	For EMI tests
	Surface density		1.05 g/cm²	Calculated	For CAST tests

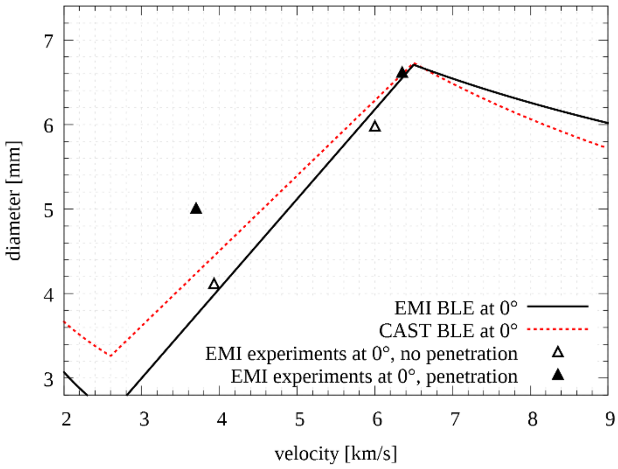

Figure 3: New ballistic limit equation at normal incidence (0° impact angle) compared to CAST ballistic limit equation with experimental data from EMI.

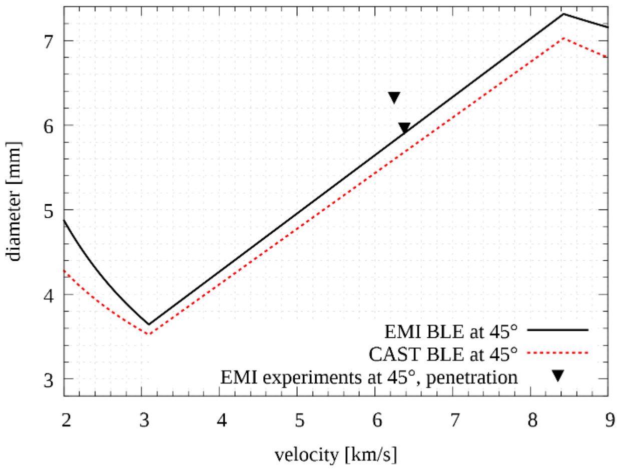

Figure 4: New ballistic limit equation at 45° impact angle compared to CAST ballistic limit equation with experimental data from EMI.

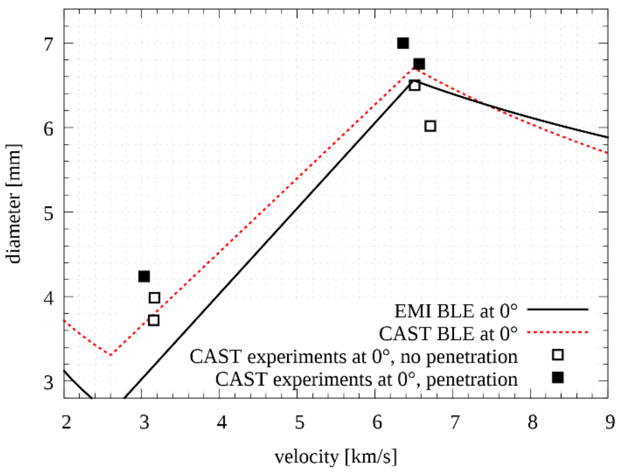

Figure 5: New ballistic limit equation at normal incidence (0° impact angle) compared to CAST ballistic limit equation with experimental data from CAST [4].

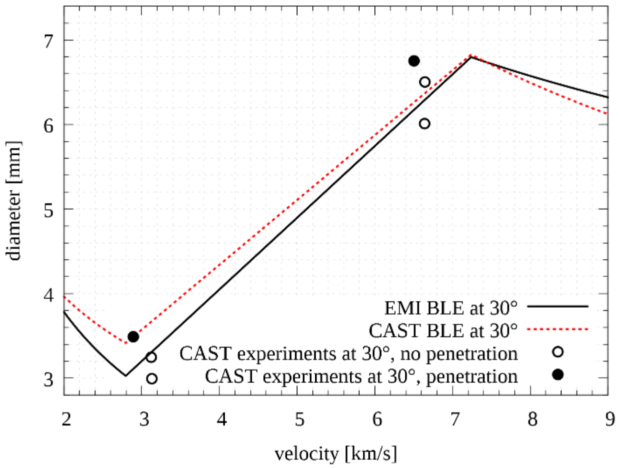

Figure 6: New ballistic limit equation at 30° impact angle compared to CAST ballistic limit equation with experimental data from CAST [4].

c_{LV} and c_{HV} were calculated to minimize the distance of the BLE to the d_p/d_{c} ratios of significant experiments. One important constraint was that the resulting BLE shall be conservative, i. e. all perforation datapoints to be above the BL curve. Experiments were considered significant when close to the ballistic limit. This includes EMI experiments 5807, 5810, 5817 and CAST experiments SW2-5 and SW2-8. From this data, $c_{\mathrm{LV}} = 2.0$ and $c_{\mathrm{HV}} = 0.49$. Figures 3 and 4 show the ballistic limit equation compared to the experimental data from Fraunhofer EMI. Figures 5 and 6 show the ballistic limit equation compared to the experimental data from CAST.

4.2.2 Discussion

The new ballistic limit equation is conservative at low impact velocities at 0° impact angle. A comparable phenomenon has been observed before for the ESA Columbus debris shield and the NASA SW shield [6]. There it was found that "the evolution of the ballistic limit with the impact angle is almost constant from 0 to 45 degrees and then increases from 45 to 60 degrees." Until today, this effect has not been investigated in detail.

The new BLE, similar to the ESA Columbus Module BLE and the NASA stuffed Whipple shield BLE, utilizes the common linear interpolation in the shatter velocity region. Investigations on dual wall all-aluminum Whipple shields indicate that the fragmentation process and phase transitions of the impacting particle lead to a more complex and nonlinear relationship of the critical diameter with velocity [37, 38]. Those investigations conclude that the linear interpolation can be considered conservative. For stuffed Whipple shields, no similar investigations exists. However, the effects described in refs. [37, 38] for all-aluminum Whipple shields are also relevant for stuffed Whipple shields with aluminum bumpers. Also, for oblique impacts, the shatter velocity regime moves to higher impact velocities, because the velocity component towards the surface normal becomes relevant. Therefore, fragmentation and phase transition effects may be responsible for a part of the impact behavior observed for stuffed Whipple shields at oblique impact angles. For the new BLE, the linear interpolation is adopted due to lack of alternatives, until more investigations in this velocity region motivate a different approach.

Regarding overall performance of the BLE, from Figures 3, 5 and 6 it is evident that the CAST BLE is less conservative in the velocity regime between ca. 1 km/s and ca. 7 km/s for impact angles up to about 30°. For the more relevant impact angle of 45°, the CAST BLE is more conservative than the newly developed BLE.

Figure 7 shows the projectile diameter normalized with the critical diameter as predicted by the new ballistic limit equation. Overall, the ballistic limit equation is conservative, i. e. there is no datapoint with penetration above the ballistic limit curve. The comparatively large values for velocities around 3 km/s are owing to the effect described above, which are not captured by the new BLE.

Figure 8 shows the projectile diameter normalized with the critical diameter, but as predicted by the CAST ballistic limit equation. Overall, this ballistic limit equation is also conservative, i. e. there is no datapoint with penetration above the ballistic limit curve. The scatter at velocities around 3 km/s is less than for the new BLE. From a matter of simple comparison, the CAST BLE seems to perform better than the new BLE. Since the amount of experimental datapoints is rather limited, it is proposed to stick to the new BLE, as the basic pattern of this BLE is based on more experimental data.

Considering the anticipated orbit of the Chinese space station, most impacts will likely be in the hypervelocity regime, cf. Figure 9. In this regime, the CAST BLE is more conservative than the new BLE. This is especially true for impact velocities much higher than 7 km/s due to the different velocity exponent, cf. Section 2.1.5. From a crew safety point of view, the impact risk analysis will yield conservative results for both the new BLE and the CAST BLE.

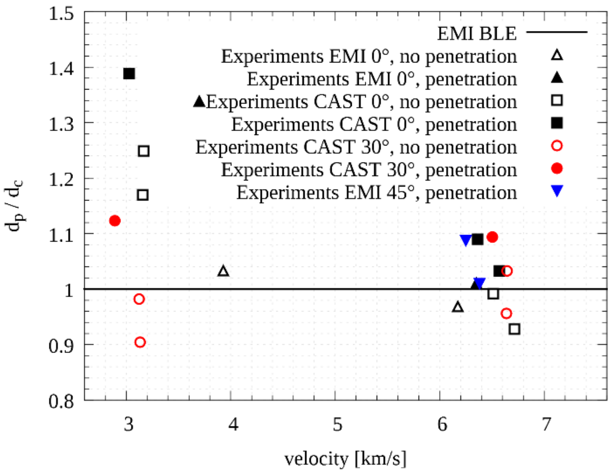

Figure 7: Ratio of projectile diameter d_p to BLE predicted critical diameter d_c for the new BLE for all experiments in Table 3. All penetrations are above the BLE, indicating conservativeness.

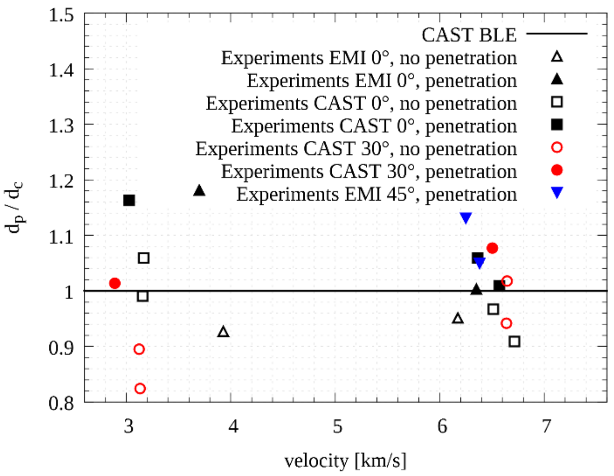

Figure 8: Ratio of projectile diameter d_p to BLE predicted critical diameter d_c for the CAST BLE for all experiments in Table 3. All penetrations are above the BLE, indicating conservativeness.

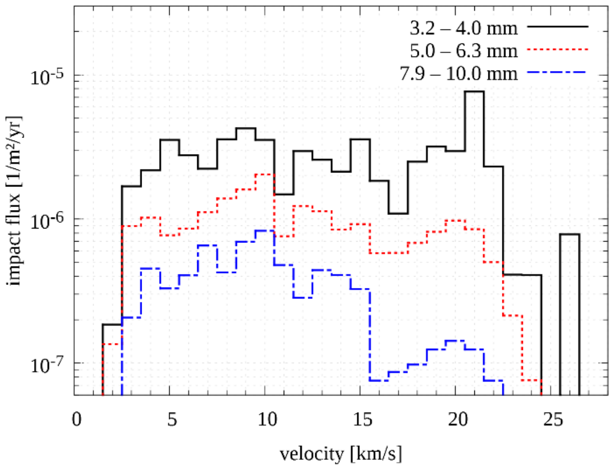

Figure 9: Impact flux (on a logarithmic scale) according to MASTER 2009 [39] for the year 2018 for three important impactor size bins. Since the orbit parameters for the new Chinese space station are not known, the orbit of Tiangong-2 was used (semi-major axis 6763 km, eccentricity 0.0001998, inclination 42.8°, right ascension of the ascending node 69.6504°, argument of perigee 88.5323°).

4.2.3 Application to other Chinese shields

The new BLE can also be applied to the other two shields described in ref. [4]. When assuming the same surface density for a beta cloth layer, s_b calculates to 0.439 g/cm² for SW1 and 0.386 g/cm² for SW3. It is found that the new BLE is close to the performance level of SW1, but not well suited for SW3 (overly conservative in the hypervelocity regime, but non-conservative for 30° experiments in the low velocity regime). Since the investigations of those two shields was not a concern for the work presented, no ballistic limit plots are given here. Also, no further investigation in those phenomena was performed.

4.3 Ballistic limit equation for the two-layer shield

Three impact tests were performed on the two-layer shield at velocities between 7.1 and 7.9 km/s. The ballistic limit at those velocities was determined experimentally. Due to lack of samples and testing time available, no ballistic limit was determined at other velocities. The shield layout resembles the standard Whipple configuration. Therefore, the Christiansen Whipple shield ballistic limit equation from ref. [40] was applied to this target. An equivalent bumper thickness of 0.079 cm was calculated from the surface density of the stuffing (0.2133 g/cm²) using a density of 2.7 g/cm³. All other properties required are either identical to the three-layer shield, or measured values for the two-layer shield.

Figure 10 shows the available experimental data together with the unadjusted Christiansen Whipple shield equation. The shield performance is worse than that of a full-aluminum shield with equal surface density.

Experimental data suggests that this is due to a worse fragmentation of the projectile at the fabric bumper than what would be expected from a full-aluminum bumper. Also, even at 7.94 km/s, impact craters are visible on the rear wall. This suggests that the transition velocity for this bumper is well above 7 km/s. Therefore, applicability of the Christiansen Whipple shield equation is questionable. With the small amount of test data available for this shield type, no further conclusions can be drawn.

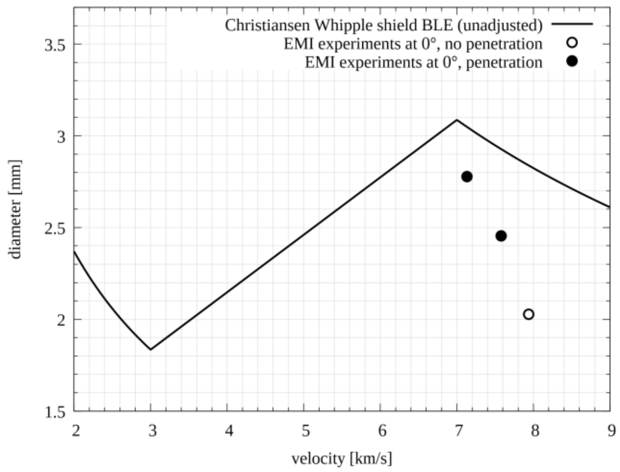

Figure 10: Experimental data for the two-layer shield with unadjusted Christiansen Whipple shield equation.

5 Conclusions

Nine successful hypervelocity impact tests were performed on shield samples designated to be used onboard the future Chinese space station. Two types of shields were impact tested: a three-layer shield and a two-layer shield.

For the three-layer shield, a new ballistic limit equation (BLE) was derived, based on the NASA stuffed Whipple shield BLE [13], effectively utilizing the experimental knowledge that is already contained therein. The new BLE is conservative, i. e. there is no data point with penetration above the ballistic limit curve. Especially at low impact angles and low impact speeds, the new BLE is overly conservative. Similar effects have been observed before for the ESA Columbus debris shield and the NASA SW shield [6]. The reason for this could not be clarified due to the limited experimental dataset available, but may be related to the behavior in the shatter regime [37, 38]. The second BLE available for this shield, the CAST BLE from [4], also yields conservative results.

Considering the anticipated orbit of the Chinese space station, most impacts will likely be in the hypervelocity regime. In this regime, the CAST BLE is more conservative than the new BLE. From a crew safety point of view, the impact risk analysis will yield conservative results for both the new BLE and the CAST BLE.

All conclusions are somewhat restrained by the limited amount of impact data available. Especially at 45° impact angle, more data points would be beneficial to further substantiate the conclusions.

The two-layer shield layout resembles the standard Whipple configurations. However, the comparison to the standard Christiansen Whipple shield ballistic limit equation [40] shows that the performance of this shield is worse than that of a full-aluminum shield with equal surface density. Experimental data suggests that this is due to a worse fragmentation of the projectile at the fabric bumper than what would be expected from a full-aluminum bumper. Also, even at 7.94 km/s, impact craters are visible on the rear wall, suggesting that the transition velocity for this bumper is significantly above the 7 km/s usually considered for aluminum on aluminum impacts. Therefore, the applicability of the Christiansen Whipple shield equation is not given. Additional test data for this shield type is required for further conclusions.

Declaration of interest

All authors declare no conflict of interest.

Acknowledgements

The authors would like to acknowledge the excellent work of the laboratory personnel, especially of Mr. Hans-Peter Osterer who operated the accelerator during the impact tests.

Funding sources

The research described in this article was carried out under a program of and funded by the European Space Agency under contract no. 4000121561/17/NL/PG/eg. ESA was not involved in the collection, analysis or interpretation of the data, or in the decision to submit this article for publication. The view expressed in this publication can in no way be taken to reflect the official opinion of the European Space Agency.

Appendix A. Derivation of the Chinese ballistic limit equation

The derivation procedure of the Chinese ballistic limit equation is described in detail in ref. [18]. Since this article is in Chinese, the method is outlined in the following. The variables were re-named to conform to the nomenclature in this publication. For the rationale and in case of doubt, the reader is kindly asked to refer to ref. [18].

The ballistic limit is described separately in each of the three velocity regimes defined above in section 2.1. The transition velocities between the three regimes are taken from ref. [13] and are stated above in sections 2.1.1 and 2.1.3. For the intermediate velocity regime, the critical diameter is assumed to linearly depend on the velocity as outlined in section 2.1.

The protective capability of the stuffed Whipple shield is described by the equivalent thickness t_{eq} of a single wall shield, made from the rear wall material, which achieves the same protection as the stuffed Whipple shield. t_{eq} is derived independently for the low velocity and the hypervelocity regime as $t_{\mathrm{eq,LV}}$ and $t_{\mathrm{eq,HV}}$. The critical diameter d_{c} is then assumed to depend on this equivalent single wall thickness t_{eq}, the single wall density ρ_{w}, the single wall yield strength σ_{w}, the projectile density ρ_{p}, and the normal projectile velocity

$$v_{\mathrm{n}} = v \cdot \cos(\theta) \quad . \tag{A.1}$$

Table 2 in ref. [18] lists the physical dimensions (in terms of length, time and mass) of those variables. Assuming dimensional homogeneity and choosing d_{c}, v_{n} and ρ_{p} as base quantities, the ballistic limit equation for the equivalent single wall can then be written as

$$\frac{d_{\mathrm{c}}}{t_{\mathrm{eq}}} = f_1\left(\frac{\rho_{\mathrm{w}}}{\rho_{\mathrm{p}}}, \frac{\rho_{\mathrm{p}} \cdot v_{\mathrm{n}}^2}{\sigma_{\mathrm{w}}}\right) \quad , \tag{A.2}$$

with a to be defined function f_1, cf. equation (7) in ref. [18]. It is further assumed that the function f_1 can be written as

$$\frac{d_{\mathrm{c}}}{t_{\mathrm{eq}}} = c_1 \cdot \left(\frac{\rho_{\mathrm{w}}}{\rho_{\mathrm{p}}}\right)^{c_2} \cdot \left(\frac{\rho_{\mathrm{p}} \cdot v_{\mathrm{n}}^2}{\sigma_{\mathrm{w}}}\right)^{c_3} \quad , \tag{A.3}$$

with to be determined coefficients c_1, c_2 and c_3, cf. equation (8) in ref. [18].

The equivalent thickness t_{eq} is assumed to depend on the rear wall thickness t_{w}, scaled thicknesses of all individual layers t'_{b}, t'_{sb} and t'_{sk}, and the spacing S, cf. equation (6) in ref. [18]. For each layer, the scaled thickness is assumed to depend on the actual thickness, the density and the yield strength. The influence of the density on the scaled thickness is assumed to be linear, and the influence of yield strength on the scaled thickness is assumed to follow a power law function. Thus (remembering $t \cdot \rho = s$):

$$t'_{\mathrm{b}} = t_{\mathrm{b}} \cdot \frac{\rho_{\mathrm{b}}}{\rho_{\mathrm{w}}} \cdot \left(\frac{\sigma_{\mathrm{b}}}{\sigma_{\mathrm{w}}}\right)^{c_{\mathrm{b}}} \quad , \quad t'_{\mathrm{sb}} = \frac{s_{\mathrm{sb}}}{\rho_{\mathrm{w}}} \cdot \left(\frac{\sigma_{\mathrm{sb}}}{\sigma_{\mathrm{w}}}\right)^{c_{\mathrm{sb}}} \quad , \quad t'_{\mathrm{sk}} = \frac{s_{\mathrm{sk}}}{\rho_{\mathrm{w}}} \cdot \left(\frac{\sigma_{\mathrm{sk}}}{\sigma_{\mathrm{w}}}\right)^{c_{\mathrm{sk}}} \quad . \tag{A.4}$$

In the low velocity regime, the following assumptions are made: The influence of the spacing S is neglected since no fragmentation and thus no spread of projectile fragments is assumed. $t_{\mathrm{eq,LV}}$ is assumed to be the sum of scaled thicknesses of the individual layers:

$$t_{\mathrm{eq,LV}} = t_{\mathrm{w}} + t'_{\mathrm{b}} + t'_{\mathrm{sb}} + t'_{\mathrm{sk}} \quad , \tag{A.5}$$

cf. equation (10) in ref. [18]. The yield strength power law coefficients c_{b}, c_{sb} and c_{sk} are assumed to be identical for all materials involved. The difference between bumper plate density and rear wall density can be neglected. From those assumptions,

$$d_{\mathrm{c,LV}} = a_1 \left(t_{\mathrm{w}} + t_{\mathrm{b}} \left(\frac{\sigma_{\mathrm{b}}}{\sigma_{\mathrm{w}}} \right)^{a_2} + \frac{s_{\mathrm{sb}}}{\rho_{\mathrm{w}}} \left(\frac{\sigma_{\mathrm{sb}}}{\sigma_{\mathrm{w}}} \right)^{a_2} + \frac{s_{\mathrm{sk}}}{\rho_{\mathrm{w}}} \left(\frac{\sigma_{\mathrm{sk}}}{\sigma_{\mathrm{w}}} \right)^{a_2} \right) \left(\frac{\rho_{\mathrm{w}}}{\rho_{\mathrm{p}}} \right)^{a_3} \left(\frac{\rho_{\mathrm{p}} \cdot v_{\mathrm{n}}^2}{\sigma_{\mathrm{w}}} \right)^{a_4} \quad , \tag{A.6}$$

which is equation (3).

In the hypervelocity regime, the following assumptions are made: The influence of material strength of all layers on the equivalent plate thickness $t_{\mathrm{eq,HV}}$ can be neglected. The influence of the material densities can be neglected. The influence of the bumper plate thickness t_{b}, the rear wall thickness t_{w} and the spacing S can be described by a combined thickness proportional to the product $t_w^{c_4} \cdot t_b^{c_5} \cdot S^{1-c_4-c_5}$. The influence of the stuffing thicknesses t_{sb} and t_{sk} can be described by a combined thickness proportional to the product $t_{\mathrm{sb}}^{c_6} \cdot t_{\mathrm{sk}}^{1-c_6}$. $t_{\mathrm{eq,HV}}$ is the sum of those two thicknesses:

$$t_{\mathrm{eq,HV}} = c_7 \left(t_{\mathrm{b}}^{c_4}\, t_{\mathrm{w}}^{c_5}\, S^{1-c_4-c_5} + c_8\, t_{\mathrm{sb}}^{c_6}\, t_{\mathrm{sk}}^{1-c_6} \right) \quad , \tag{A.7}$$

cf. equation (13) in ref. [18]. From those assumptions (remembering $s = t \cdot \rho$ again),

$$d_{\mathrm{c,HV}} = a_5 \left(t_{\mathrm{b}}^{a_6}\, t_{\mathrm{w}}^{a_7}\, S^{1-a_6-a_7} + a_8 \left(\frac{s_{\mathrm{sb}}}{\rho_{\mathrm{w}}} \right)^{a_9} \left(\frac{s_{\mathrm{sk}}}{\rho_{\mathrm{w}}} \right)^{1-a_9} \right) \left(\frac{\rho_{\mathrm{w}}}{\rho_{\mathrm{p}}} \right)^{a_{10}} \left(\frac{\rho_{\mathrm{p}} \cdot v_{\mathrm{n}}^2}{\sigma_{\mathrm{w}}} \right)^{a_{11}} \quad , \tag{A.8}$$

which is equation (4).

Appendix B. Derivation of parameters for the Chinese ballistic limit equation

The ballistic limit equation derived in ref. [18] (see appendix A above) contains 11 parameters (a_1 to a_{11}) that need to be identified for a specific shield. Zheng et al. [4] decided to use a differential evolution algorithm for this purpose. This type of algorithm was first described by Storn and Price [20]. The application of the algorithm to the Chinese BLE is described in ref. [19]. Since this article is in Chinese, the algorithm is briefly described here. Again, some variables were re-named to conform to the nomenclature in this publication. For the rationale and in case of doubt, the reader is kindly asked to refer to ref. [19].

For the initial population, N_{P} random vectors within the lower bounds a_i^{L} and the upper bounds a_i^{U} were generated (equation (1) in ref. [19]):

$$a_{ij}(0) = a_j^{\mathrm{L}} + \mathrm{rand}(0{,}1)\left(a_j^{\mathrm{U}} - a_j^{\mathrm{L}}\right), \qquad i = 1{,}2{,}\cdots, N_{\mathrm{P}}\,, \qquad j = 1{,}2{,}\cdots{,}11 \tag{B.1}$$

with $\mathrm{rand}(0{,}1)$ being an individual random variable between 0 and 1 for every pair of i and j. A population of $N_{\mathrm{P}} = 60$ was chosen. It is noted that larger populations result in more stable results. The lower and upper bounds a_i^{L} and a_i^{U} were calculated from the starting set of parameters $a_i^{\mathrm{S}} = [0.6, 0.3, 0.2, -0.3, 1, 0.3, 0.4, 1.2, 0.3, 0.2, -0.25]$ (also given in table 2 of ref. [19]) as $a_i^{\mathrm{L}} = 0.5 \cdot a_i^{\mathrm{S}}$ and $a_i^{\mathrm{U}} = 1.5 \cdot a_i^{\mathrm{S}}$.

Mutant vectors were generated according to equation (2) in ref. [20], which is equal to equation (2) in ref. [19], using an amplification factor $F = 0.5$. Mutant vectors that were not within the lower and upper bounds were discarded. Crossovers were generated according to equation (4) in ref. [20], which is equal to equation (3) in ref. [19], using a crossover constant $C_R = 0.3$.

To define the cost function $F(a_i)$ for evaluation of the fitness of the population vectors, three values were calculated for each vector a_i, using the experimental data: the fraction of correct predictions for all tests (including perforation or no perforation of the rear wall), the fraction of correct predictions for the tests that caused perforation of the rear wall, and the negative sum of the squared relative distances between the projectile diameter and ballistic limit diameter. As cost function, the maximum of these three functions was used, see equation (11) in ref. [20].

To obtain the optimum values, 100 generations were calculated. The vector with the smallest value of the cost function was used as final parameter set.

References

[1] ESA declares end of mission for Envisat. Space Research Today. 2012;184:13-14. doi: 10.1016/j.srt.2012.07.012.

[2] Whipple FL. Meteorites and space travel. The Astronomical Journal. 1947;52(1161):131. doi: 10.1086/106009.

[3] Christiansen EL, Nagy K, Lear DM, Prior TG. Space station MMOD shielding. Acta Astronautica. 2009;65(7-8):921-929. doi: 10.1016/j.actaastro.2008.01.046.

[4] Zheng S, Yan J, Weiwei G. Impact characterization of stuffed whipple for China Space Station. In: Flohrer T,F Schmitz, editors: Proceedings of the 7th European Conference on Space Debris; Darmstadt: ESA Space Debris Office; 2017.

[5] Zheng S, Yan J, Shan L, Jiang C. Research on shield for space station from meteoroid and orbital debris. In: Proceedings of the 64th International Astronautical Congress; Beijing, China; 2013. IAC-13,A6,3,4,x17523.

[6] Destefanis R, Faraud M, Trucchi M. Columbus debris shielding experiments and ballistic limit curves. International Journal of Impact Engineering. 1999;23:181-192. doi: 10.1016/S0734-743X(99)00071-8.

[7] Ryan S, Christiansen EL. Micrometeoroid and Orbital Debris (MMOD) Shield Ballistic Limit Analysis Program: NASA JSC; 2009. NASA JSC TM-2009-214789.

[8] Schneider E, Stilp A, Bureo R, Lambert M. Micrometeorite and space debris simulation for Columbus hull components. International Journal of Impact Engineering. 1990;10:499-508. doi: 10.1016/0734-743X(90)90083-8.

[9] Schneider E, Stilp A. Meteoroid/debris simulation at Ernst-Mach-Institut (EMI) - experimental methods and recent results. In: Flury W, editor: Proceedings of the 1st European Conference on Space Debris; Darmstadt; 1993. p. 401-404. ESA SD-01.

[10] Schneider EE, Schäfer FK, Destefanis R, Lambert M. Advanced shields for manned space modules. In: Proceedings of the 55th International Astronautical Congress 2004; Vancouver, Canada; 2004. IAC-04-IAA.5.12.2.01.

[11] Thoma K, Schäfer F, Hiermaier S, Schneider E. An approach to achieve progress in spacecraft shielding. Advances in Space Research. 2004;34:1063-1075. doi: 10.1016/j.asr.2003.03.034.

[12] Christiansen EL, Crews JL, Williamsen JE, Robinson JH, Nolen AM. Enhanced meteoroid and orbital debris shielding. International Journal of Impact Engineering. 1995;17:217-228. doi: 10.1016/0734-743X(95)99848-L.

[13] Christiansen EL, Arnold J, Davis A, Hyde J, Lear D, Liou J-C, Lyons F, Prior T, Ratliff M, Ryan S, Giovane F, Corsaro B, Studor G. Handbook for designing MMOD protection: NASA Johnson Space Center; 2009. NASA/TM-2009-214785.

[14] Christiansen EL, Kerr JH. Ballistic limit equations for spacecraft shielding. International Journal of Impact Engineering. 2001;26:93-104. doi: 10.1016/S0734-743X(01)00070-7.

[15] Christiansen EL. Advanced meteoroid and debris shielding concepts. In: Proceedings of the AIAA/NASA/DOD Orbital Debris Conference; Baltimore, MD, USA; 1990. doi: 10.2514/6.1990-1336.

[16] Christiansen EL, Kerr JH. Mesh double-bumper shield: A low-weight alternative for spacecraft meteoroid and orbital debris protection. International Journal of Impact Engineering. 1993;14(1-4):169-180. doi: 10.1016/0734-743X(93)90018-3.

[17] Christiansen EL. Meteoroid/Debris Shielding: NASA Johnson Space Center; 2003. NASA TP-2003-210788.

[18] Yao G, Zheng S, Yan J, Jia G. General form determination of ballistic limit equation about stuffed Whipple shield (填充式防护结构弹道极限方程形式建模). Space Debris Research (空间碎片研究). 2017;17(1):29-33. (In Chinese).

[19] Jia G, Yao G, Zhang S. Differential evolution optimization for stuffed Whipple shield ballistic limit equations (填充式防护结构弹道极限方程的差异演化优化). Journal of Beijing University of Aeronautics and Astronautics (北京航空航天大学学报). 2018;44(7):1489-1495. doi: 10.13700/j.bh.1001-5965.2017.0515. (In Chinese).

[20] Storn R, Price K. Differential evolution – A simple and efficient heuristic for global optimization over continuous spaces. Journal of Global Optimization. 1997;11(4):341-359. doi: 10.1023/A:1008202821328.

[21] 3M. 3M Nextel ceramic fibers and textiles : Technical reference guide: 3M dvanced Materials Division; 2016.

[22] Fiore V, Scalici T, Di Bella G, Valenza A. A review on basalt fibre and its composites. Composites Part B: Engineering. 2015;74:74-94. doi: 10.1016/j.compositesb.2014.12.034.

[23] Ha Y, Pang BJ, Guan GS, Zhang W. Damage of high velocity impact on basalt fiber hybrid woven-Al Whipple shield (玄武岩纤维布Whipple防护结构超高速撞击损伤分析). Journal of Harbin Institute of Technology (哈尔滨工业大学学报). 2007;39(5):779-785. (In Chinese).

[24] Zhang B, Ha Y, Deng Y, Pang B. The optimal structural design of stuffed shields with basalt and kevlar fiber clothes against hypervelocity impacting (超高速撞击玄武岩及Kevlar纤维布填充防护结构研究). Chinese Journal of Solid Mechanics (固体力学学报). 2012;33(5):533-540. (In Chinese).

[25] Jia G, Ha Y, Pang B, Guan G, Zu S. Ballistic limit and damage properties of basalt/Kevlar stuffed shield (玄武岩/Kevlar纤维布填充防护结构撞击极限及损伤特性). Explosion and Shock Waves (爆炸与冲击). 2016;36(4):433-440. doi: 10.11883/1001-1455(2016)04-0433-08. (In Chinese).

[26] Wikipedia. Basalt fiber, https://en.wikipedia.org/wiki/Basalt_fiber; 2018 [accessed 2018-03-07]

[27] Wikipedia. Basaltfaser, https://de.wikipedia.org/wiki/Basaltfaser; 2018 [accessed 2018-03-08]

[28] Putzar R, Schäfer F. Experimental space debris simulation at EMI's calibre 4 mm two-stage light gas gun. In: Lacoste H, editor: Proceedings of the 5th European Conference on Space Debris; Darmstadt, Germany: ESA Publications Division; 2009. ESA SP-672.

[29] Stilp A. Review of modern hypervelocity impact facilities. International Journal of Impact Engineering. 1987;5:613-621. doi: 10.1016/0734-743X(87)90076-5.

[30] Lexow B, Wickert M, Thoma K, Schäfer F, Poelchau MH, Kenkmann T. The extra-large light-gas gun of the Fraunhofer EMI: Applications for impact cratering research. Meteoritics & Planetary Science. 2013;48(1):3-7. doi: 10.1111/j.1945-5100.2012.01427.x.

[31] Putzar R, Zheng S, An J, Hovland S. A stuffed Whipple shield for the Chinese space station – Post-impact target photographs. Mendeley Data, v2. 2019. doi: 10.17632/2f74svfv5p.2.

[32] Zhang H, Wu G, Yan Z, Pei F, Li J, Wang W, Li Y. Fatigue fracture behavior of 5A06 aluminum alloy and its welded joint. The Chinese Journal of Nonferrous Metals. 2013;23(2):327-335.

[33] Guo N, Fu Y, Wang Y, Meng Q, Zhu Y. Microstructure and mechanical properties in friction stir welded 5A06 aluminum alloy thick plate. Materials and Design. 2017;113:273-283. doi: 10.1016/j.matdes.2016.10.030.

[34] Zeng Z, Wu X, Yang M, Peng B. Welding distortion prediction in 5A06 aluminum alloy complex structure via inherent strain method. Metals. 2016;6(9):214. doi: 10.3390/met6090214.

[35] Ren P, Zhang W. Underwater shock response of air-backed thin aluminum alloy plates: An experimental and numerical study. Journal of Physics: Conference Series. 2014;500:182034. doi: 10.1088/1742-6596/500/18/182034.

[36] Gongshun G, Baojun P, Wei Z, Yue H. Crater distribution on the rear wall of AL-Whipple shield by hypervelocity impacts of AL-spheres. International Journal of Impact Engineering. 2008;35(12):1541-1546. doi: 10.1016/j.ijimpeng.2008.07.028.

[37] Ryan S, Bjorkman M, Christiansen EL. Whipple shield performance in the shatter regime International Journal of Impact Engineering. 2011;38(6):504-510. doi: 10.1016/j.ijimpeng.2010.10.022.

[38] Hopkins AK, Lee TW, Swift HF. Material phase transformation effects upon performance of spaced bumper systems. Journal of Spacecraft and Rockets. 1972;9(5):342-345. doi: 10.2514/3.61684.

[39] Flegel S, Gelhaus J, Möckel M, Wiedemann C, Kempf D, Oswald M, Stabroth S, Alagöz C. MASTER-2009 software user manual. Braunschweig: TU Braunschweig, Institute of Aerospace Systems; 2011. RFQ No 21705/08/D/HK.

[40] Christiansen EL. Design and performance equations for advanced meteoroid and debris shields. International Journal of Impact Engineering. 1993;14:145-156. doi: 10.1016/0734-743X(93)90016-Z.